








Article

Efficient Delivery of DNA Using Lipid Nanoparticles

Lishan Cui ^{1,†} , Serena Renzi ^{2,†}, Erica Quagliarini ², Luca Digiacomo ² , Heinz Amenitsch ³ , Laura Masuelli ⁴, Roberto Bei ⁵ , Gianmarco Ferri ⁶, Francesco Cardarelli ⁶ , Junbiao Wang ¹ , Augusto Amici ¹, Daniela Pozzi ², Cristina Marchini ^{1,*} and Giulio Caracciolo ^{2,*} 

¹ School of Biosciences and Veterinary Medicine, University of Camerino, 62032 Camerino, Italy

² NanoDelivery Lab, Department of Molecular Medicine, Sapienza University of Rome, 00161 Rome, Italy

³ Institute of Inorganic Chemistry, Graz University of Technology, 8010 Graz, Austria

⁴ Department of Experimental Medicine, “Sapienza” University of Rome, 00161 Rome, Italy

⁵ Department of Clinical Sciences and Translational Medicine, University of Rome “Tor Vergata”, 00133 Rome, Italy

⁶ National Enterprise for NanoScience and NanoTechnology (NEST), Scuola Normale Superiore, 56127 Pisa, Italy

* Correspondence: cristina.marchini@unicam.it (C.M.); giulio.caracciolo@uniroma1.it (G.C.)

† These authors contributed equally to this work.

Abstract: DNA vaccination has been extensively studied as a promising strategy for tumor treatment. Despite the efforts, the therapeutic efficacy of DNA vaccines has been limited by their intrinsic poor cellular internalization. Electroporation, which is based on the application of a controlled electric field to enhance DNA penetration into cells, has been the method of choice to produce acceptable levels of gene transfer in vivo. However, this method may cause cell damage or rupture, non-specific targeting, and even degradation of pDNA. Skin irritation, muscle contractions, pain, alterations in skin structure, and irreversible cell damage have been frequently reported. To overcome these limitations, in this work, we use a microfluidic platform to generate DNA-loaded lipid nanoparticles (LNPs) which are then characterized by a combination of dynamic light scattering (DLS), synchrotron small-angle X-ray scattering (SAXS), and transmission electron microscopy (TEM). Despite the clinical successes obtained by LNPs for mRNA and siRNA delivery, little is known about LNPs encapsulating bulkier DNA molecules, the clinical application of which remains challenging. For in vitro screening, LNPs were administered to human embryonic kidney 293 (HEK-293) and Chinese hamster ovary (CHO) cell lines and ranked for their transfection efficiency (TE) and cytotoxicity. The LNP formulation exhibiting the highest TE and the lowest cytotoxicity was then tested for the delivery of the DNA vaccine pVAX-hECTM targeting the human neoantigen HER2, an oncoprotein overexpressed in several cancer types. Using fluorescence-activated cell sorting (FACS), immunofluorescence assays and fluorescence confocal microscopy (FCS), we proved that pVAX-hECTM-loaded LNPs produce massive expression of the HER2 antigen on the cell membrane of HEK-293 cells. Our results provide new insights into the structure–activity relationship of DNA-loaded LNPs and pave the way for the access of this gene delivery technology to preclinical studies.

Keywords: DNA vaccines; lipid nanoparticles; HER2



Citation: Cui, L.; Renzi, S.; Quagliarini, E.; Digiacomo, L.; Amenitsch, H.; Masuelli, L.; Bei, R.; Ferri, G.; Cardarelli, F.; Wang, J.; et al. Efficient Delivery of DNA Using Lipid Nanoparticles. *Pharmaceutics* **2022**, *14*, 1698. <https://doi.org/10.3390/pharmaceutics14081698>

Academic Editor: Lídia Maria Diogo Gonçalves

Received: 7 July 2022

Accepted: 28 July 2022

Published: 15 August 2022

Publisher's Note: MDPI stays neutral with regard to jurisdictional claims in published maps and institutional affiliations.



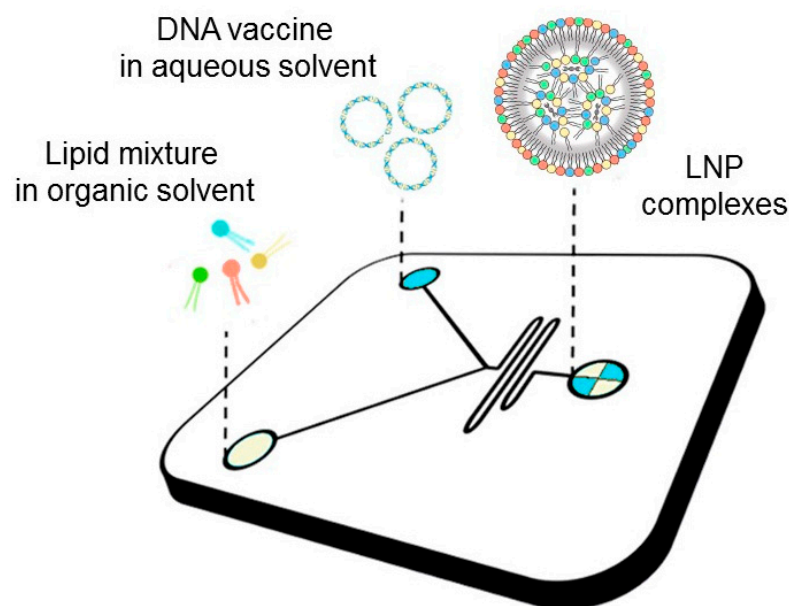
Copyright: © 2022 by the authors. Licensee MDPI, Basel, Switzerland. This article is an open access article distributed under the terms and conditions of the Creative Commons Attribution (CC BY) license (<https://creativecommons.org/licenses/by/4.0/>).

1. Introduction

Despite the massive involvement of resources in cancer studies and in the development of potential therapeutic strategies, cancer is still one of the main causes of death worldwide [1]. The conventional approaches in cancer therapy, such as chemotherapy, radiotherapy, and surgery, are often effective in early-stage tumors but not in those diagnosed in advanced stages. The temporary suspension of screening programs caused by the COVID-19 pandemic exacerbated this trend [2]. The non-specific targeting of both tumoral and healthy cells observed in traditional chemotherapies causes side effects that have significantly evolved over the last decades [3]. Recently, immunotherapy has been investigated

as an alternative strategy to most traditional therapies. It aims at boosting patient immunity or promote tumor-cell killing by targeting specifically immunomodulator pathways [4]. Vaccination, one of the most successful strategies for the prevention of infectious diseases, emerged as an attractive immunotherapeutic approach against cancer [5]. DNA vaccines consist of plasmid DNA (pDNA) of bacterial origin which encodes for the target antigen that can elicit both humoral and cell-mediated immunity. At the formulation level, DNA vaccines hold several benefits over whole pathogen (i.e., attenuated and inactivated viral vaccines) or protein-based vaccines, such as simple and rapid manufacturing processes or the easy manipulation of the encoded antigen by DNA engineering [6]. Additionally, the thermostability of DNA vaccines tackles the complications linked to cold chain [7] maintenance, which instead is essential for less stable vaccines (e.g., mRNA-based vaccines) to avoid the inactivation during supply. Despite many clinical trials of DNA vaccines for cancers now being underway, none have been licensed for human use thus far. The biggest hurdle for their clinical translation is the difficulty in efficient delivery to the cell machinery. Viral vectors are associated with many risks such as genome integration and possible host rejection. Nonviral DNA delivery systems employ either chemical or physical approaches. The most investigated physical method is electroporation, which is based on the application of a controlled electric field to enhance DNA penetration into cells and generates high levels of gene transfer in vivo [8]. However, despite its versatility and lower amount of required DNA, this method may cause cell damage or rupture, non-specific targeting, and even degradation of pDNA. Conversely, nanoparticles (NPs) hold great promise for efficient DNA delivery. Such nanodelivery systems protect the nucleic acid payload from degradation, favor versatile formulation strategies to cross the barriers of cell internalization, enhance specific immune cell targeting by surface modifications, and exploit pH-sensitive shells to improve endosomal escape. Cationic lipid–DNA complexes (lipoplexes) have been largely employed as gene delivery systems since cationic lipids allow an easy complexation with negatively charged pDNA. The conventional method for manufacturing lipoplexes is the bulk mixing process that leads to heterogeneous large-size vesicles and requires an additional down-sizing technique (i.e., sonication or extrusion) to achieve the desired particle size [9]. To overcome this limitation, microfluidic mixing has emerged as a robust, scalable, and highly reproducible technique to encapsulate gene therapeutics. The result of the mixing process is a lipid NP (LNP) with the genetic material encapsulated in the lipid core [9]. LNPs with different physicochemical characteristics can be achieved by adjusting several factors, such as (i) lipid composition, (ii) total lipid/DNA weight ratio, (iii) cationic lipid/DNA weight ratio, (iv) solution concentration, and (v) microfluidic operating parameters, such as the flow rate ratio (FRR) or the total flow rate (TFR) [10]. In this work, we used a microfluidic platform to generate DNA-loaded LNPs (as depicted in Figure 1) with distinct physical–chemical properties as determined by dynamic light scattering (DLS), synchrotron small-angle X-ray scattering (SAXS), and transmission electron microscopy (TEM). Previous investigations have demonstrated that multicomponent lipoplexes overcome binary lipoplexes in transfection efficiency (TE) due to a peculiar endosomal escape ability [11–14]. According to these findings, here we prepared multicomponent LNPs made of two cationic and two neutrally charged lipids.

For in vitro screening, LNPs were administered to human embryonic kidney 293 (HEK-293) and Chinese hamster ovary (CHO) cell lines and ranked for their TE and cytotoxicity. The most promising LNP formulation was loaded with the DNA vaccine pVAX-hECTM targeting the human neoantigen HER2, an oncoprotein that is overexpressed in several cancers and that represents an ideal immunogenic target for tumor vaccines [15]. Combing results from fluorescence-activated cell sorting (FACS), immunofluorescence assays, and fluorescence confocal microscopy (FCS) we demonstrated that optimized LNPs efficiently deliver pVAX-hECTM into HEK-293 cells, leading to massive expression of the HER2 antigen on the cell membrane. Our results pave the way for the development of LNP DNA vaccines and immunotherapies against cancer and other diseases.



Staggered herringbone mixer (SHM)

Figure 1. Schematic representation of the synthesis procedure of LNP DNA vaccines.

2. Materials and Methods

2.1. Microfluidic Manufacturing of LNPs

The cationic lipids 1,2-Dioleoyl-3-trimethyl-ammonium-propane (DOTAP) and (3 β -[N,N'-dimethyl-aminoethane)-carbamoyl]-cholesterol (DC-Chol), along with the two zwitterionic lipids dioleoyl phosphatidylethanolamine (DOPE) and 1,2-dioleoyl-sn-glycero-3-phosphocholine (DOPC) were obtained from Avanti Polar Lipids (Alabaster, AL, USA). The pDNA coding for firefly luciferase reporter gene (pmirGLO) was bought from (Promega, Madison, WI, USA). NanoAssemblr[®] Benchtop from Precision NanoSystems Inc. (Vancouver, BC, Canada) equipped with a Y-shape staggered herringbone micromixer was used for lipid nanoparticle (LNPs) development. Lipids were individually dissolved in ethanol (100%) at a molar ratio of 25% mol for each lipid (Table 1) and a total concentration of 12.5 mM. The pDNA expressing luciferase was dissolved in sodium acetate 25 mM, pH = 4, to obtain a final concentration of 0.2 mg/mL and 0.1 mg/mL. The two solutions were mixed in the microfluidic chip at a fixed total flow rate (TFR; 2 mL/min) and a flow rate ratio (FRR) DNA/lipid of 3:1, reducing the ethanol concentration to 25% after the micromixing. For each DNA condition (0.2 mg/mL and 0.1 mg/mL), all formulations were produced at three different lipid/DNA weight ratios (Rw = 5, 10, and 20) hereafter referred to as LNP₅, LNP₁₀, and LNP₂₀. The LNPs were subsequently purified by dialyzing against 500 mL of phosphate-buffered saline (PBS) at pH 7.4 with Slide-A-Lazer. Dialysis cassettes (0.5–3 mL, MWCO 3.5 kDa, Thermo Scientific, Rockford, AZ, USA) for 19 h. To evaluate particle stability, LNPs were stored at 4 °C for 15 days.

Table 1. Lipid composition of LNPs. Quantity of lipids expressed as a molar percentage for each LNP formulation and respective total lipid/pDNA weight ratios (Rw).

| | DOTAP (%mol) | Dc-Chol (%mol) | DOPE (%mol) | DOPC (%mol) | Rw |
|-------------------|--------------|----------------|-------------|-------------|----|
| LNP ₅ | 25 | 25 | 25 | 25 | 5 |
| LNP ₁₀ | 25 | 25 | 25 | 25 | 10 |
| LNP ₂₀ | 25 | 25 | 25 | 25 | 20 |

2.2. Plasmid Preparation

PmirGlo and the DNA vaccine pVAX-hECTM (encoding the human extracellular and transmembrane domains of the human HER2 receptor) were transformed into *E. coli* strain DH5alpha and grown in Luria–Bertani medium supplemented with kanamycin. DNA plasmids were purified using a Maxiprep kit (Qiagen, Hilden, Germany) and their concentration was determined spectrophotometrically at 260 nm.

2.3. Encapsulation Efficiency Measurements

pDNA encapsulation efficiency of LNP₁₀ and LNP₂₀ was measured by using a Quant-iT Pico-Green dsDNA assay kit (ThermoFisher Scientific, Waltham, MA, USA). All LNP samples were diluted 300-fold in TE buffer and placed on a Corning[®] 96 Well Solid Polystyrene Microplate (Sigma-Aldrich, St. Louis, MI, USA). LNPs were lysed to release the encapsulated DNA through the addition of Triton X-100 (1% volume) to each well. Control samples were not lysed and consisted of free pDNA. The reagent Quant-iT PicoGreen was added to all wells and the samples were incubated for 5 min at room temperature. Fluorescence (excitation wavelength = 475 nm, emission wavelength = 500–550 nm) was measured by using a Glomax Discover System (Promega, Madison, WI, USA). Encapsulation efficiency (EE%) was determined by measuring the fluorescence pre-lysis and post-lysis of LNPs and calculated following Equation (1):

$$\% \text{ EE} = \frac{(\text{Lysed LNP} - \text{not lysed LNP})}{\text{Lysed LNP}} \times 100 \quad (1)$$

The DNA concentration in µg/mL of LNPs was estimated using a calibration curve obtained from measurements of pDNA at different known concentrations (Figure S1 in the Supplementary Materials).

2.4. Size and Zeta-Potential Experiments

Size and zeta-potential measures were made at 25 °C by using Zetasizer Nano ZS90 (Malvern, UK). LNPs were diluted with distilled water 1:100 before the measurement. Results for size and zeta-potential of three replicates are reported as mean ± standard deviation. For particle size, we report the Z-average that is the intensity weighted mean hydrodynamic size of the particles measured by dynamic light scattering (DLS).

2.5. Synchrotron Small-Angle X-ray Scattering

Synchrotron small-angle X-ray scattering (SAXS) investigations were performed at the Austrian SAXS beamline at ELETTRA (Trieste, Italy). The calibration of the detector (Pilatus3 1 M, Dectris, Baden, Switzerland) was made by using silver behenate powder (d-spacing = 58.376 Å), q-range settled within 0.05 and 1.5 nm⁻¹, through 10 s X-ray exposure (no radiation damage was detected). The temperature was monitored in the vicinity of the capillary. The corrections for background, primary beam intensity, and detector efficiency were all included in the analysis of SAXS patterns.

2.6. Transmission Electron Microscopy

LNPs samples (8 µL) were placed on formvar–carbon-coated copper grids (EMS, Orefield, PA, USA) and let adsorb for 5 min. The resultant film was stained with a solution of 2% uranyl acetate at room temperature for 1 min. Staining solution excess was absorbed with the filter paper. Grids were air-dried for 1 h before the observation with TEM Morgagni 268D (Philips, Amsterdam, The Netherlands).

2.7. Cell Culture

The two cell lines, human embryonic kidney-293 (HEK-293) and Chinese hamster ovary (CHO), were purchased from American Type Culture Collection (ATCC, Rockville, MD, USA) and maintained in culture in Dulbecco's Modified Essential Medium (DMEM,

Gibco, Life Technologies, Carlsbad, CA, USA) enriched with 10% fetal calf serum (FCS, Gibco, Life Technologies) and 1% penicillin–streptomycin (Gibco, Life Technologies). Cells were maintained at 37 °C with 5% CO₂ under a humidified atmosphere.

2.8. Transfection Efficiency Experiments

Cells (KEK-293 or CHO) were seeded on a 96-well plate (10,000 cells/well). After 24 h cells were treated with LNPs and lipofectamineTM 3000 (Life Technologies, Carlsbad, CA, USA) with 0.33 µg pDNA/well in Optimem medium (Life Technologies, Carlsbad, CA, USA). This dose corresponds to a typical threshold for lipoplexes leading to high TE with a minor effect on cell viability [16]. After 3 h of incubation at 37 °C and 5% CO₂, DMEM 20%FBS was added to each well. After 48 h, cells were washed in PBS 1× (Phosphate-buffer saline) and lysed using lysis buffer 1× 20 µL/well. Luciferase expression was analyzed by Luciferase Assay System (Promega, Madison, WI, USA) on half of the sample (10 µL), while half (10 µL) was used to evaluate the sample protein content through Pierce BCA Assay Protein Kit (Thermo Fisher Scientific, Waltham, MA, USA) the transfection efficiency (TE) was expressed as relative light units (RLU) per mg proteins.

2.9. Cell Viability Assay

The effects of LNP with respect to LipofectamineTM 3000 (Invitrogen, Waltham, MA, USA) on cell viability were evaluated by seeding 8000 HEK-293 and CHO cells/well in 96-well plates in a complete medium. The day after, appropriate concentrations of plasmid DNA (pmirGLO) encapsulated in LNP or complexed with lipofectamine were added. After 48 h, cell viability was determined using the MTT assay (Sigma Aldrich, St. Louis, MO, USA), which is based on the conversion of tetrazolium salt [3-(4,5-dimethylthiazol-2-yl)-2,5-diphenyl-2H-tetrazolium bromide] into formazan by means of mitochondrial enzymes. The formazan crystals were dissolved using dimethyl sulfoxide (DMSO) and the well absorbance was measured at 540 nm using Multiskan Ascent 96/384 Plate Reader. Each sample was tested with eight replicates, and the experiments were performed in triplicate. The cell viability was reported as percentage of viable cells in respect to control cells. Statistical analysis was performed using a one-way ANOVA analysis of variance and Bonferroni's multiple comparison test. The data are represented as means ± SEM. The 95% confidence interval was used as the critical level for significance.

2.10. Confocal Microscope Experiments

Live-cell fluorescence imaging was performed with a Zeiss LSM 800 confocal microscope equipped with a 63X, 1.4 N.A. oil immersion objective and GaAsP detectors. Experiments were carried out at 37 °C and 5% CO₂ using an incubation chamber. Approximately 10⁵ HEK or CHO cells were seeded in a cover glass multi-well (8 wells, Sarstedt) 24 h before the experiment. Cells were incubated with LNP–Texas Red 1X for 3 h then washed 2 times with PBS and labeled with 0.1 µL of 10 mg/mL Hoechst 33,342 (ThermoFisher). Hoechst was excited with 405 nm diode laser; Texas Red was excited with 561 nm HeNe laser and its emission collected in the 570–630 nm range; 1024 × 1024 pixel images were collected. For iMSD analysis on LNP–TexasRed 1X, time-lapse series of 500 frames (256 × 256 pixels, 50 nm/pixel) with a temporal resolution of 200 ms/frame were collected using the same excitation/emission parameters described above.

2.11. iMSD Analysis

iMSD analysis of the time-lapse movies was carried out with custom scripts working on MATLAB (MathWorks Inc., Natick, MA, USA), as described in detail in Refs [17,18]. Briefly, the spatiotemporal correlation function (STCF) was calculated for each time-lapse series; 2D-Gaussian fitting of STCF provides the iMSD curve, describing the ensemble diffusion law of imaged objects. Each iMSD curve was then fitted to extract the structural-dynamic parameters: diffusion coefficient and y -axis intercept value, with the latter related to average particle size.

2.12. Immunofluorescence Analysis

HEK-293 cells were plated in a 24-well plate (1×10^5 cells/well). One day after plating, 70–90% of confluent cells were transiently transfected with 0.5 mg or 1 mg pVAX-hECTM encapsulated in LNP or complexed with Lipofectamine 3000, according to the manufacturer's instructions. Forty-eight hours after transfection, cells were fixed for 5 min with phosphate-buffered saline (PBS)–4% paraformaldehyde (Sigma, St. Louis, MO, USA). After incubation in blocking buffer (PBS–10% bovine serum albumin (BSA; Sigma, Milan, Italy) for 20 min, cells were incubated for 1 h at 37 °C with the primary antibody trastuzumab (anti-human HER2 antibody, 1:50). After washing, cells were incubated with Alexa Fluor 488-conjugated anti-human IgG secondary antibody (Invitrogen Molecular Probes, Eugene, OR, USA) at a dilution of 1:200 for 1 h at 37 °C. Finally, cells were examined under Fluorescence Microscope (Carl Zeiss GmbH, Munich, Germany) to assess membrane expression of the oncoantigen HER2.

2.13. Flow Cytometry

HEK-293 cells were plated in a 6-well plate (1×10^6 cells/well). One day after plating, 70–90% of confluent cells were transiently transfected with pVAX-hECTM encapsulated in LNPs. Forty-eight hours after transfection cells were separated into single-cell suspension and 1×10^6 cells for each experimental condition were washed in staining buffer (0.1% NaN₃, 2% FBS in PBS) and incubated with the primary antibody anti-HER2 (trastuzumab) at 4 °C for 1 h. After three washes, Alexa Fluor 488-conjugated anti-human IgG secondary antibody was added and cells were incubated for 1 h at 4 °C. Cells were washed and resuspended in PBS before the analysis performed using FACS equipped with Cell Quest software (BD Pharmingen, BD Life Sciences, San Jose, CA, USA). FlowJo software (BD Life Sciences, San Jose, CA, USA) was employed for data analysis.

3. Results and Discussion

LNPs were produced at three different lipid/DNA weight ratios (i.e., $R_w = 20, 10,$ and 5) and are hereafter referred to as LNP₅, LNP₁₀, and LNP₂₀. The choice of preparing LNPs at different R_w values is because this is an influential parameter for the physical–chemical properties of lipid-based gene delivery systems [19]. Among them, lipoplexes are the gold standard in lipid-mediated gene transfection (lipofection) [20] and were used as a reference in the following. When lipoplexes are prepared at large lipid/DNA weight ratios (that typically occur for $R_w > 10$ [21]), the moles of cationic lipids exceed those of anionic DNA. Hence, lipoplexes are positively charged, and the net cationic charge makes them efficiently interact with the negatively charged plasma membrane [22]. On the other hand, at low lipid/DNA weight ratios ($R_w < 5$) the balance between positive and negative charges results in the formation of neutrally charged complexes of large sizes that are not compatible with gene delivery purposes [23]. However, the effect of R_w on the synthetic identity of LNPs has been poorly evaluated so far. Therefore, the first step of the present investigation was a thorough characterization of LNPs in terms of size, zeta-potential, and polydispersity index (PDI). As Table S1 shows, the large size (Z-average > 400 nm) and polydispersity (PDI > 0.9) of LNP₅ made it unsuitable for gene delivery, and this formulation was therefore excluded from the following experiments. On the other side, as shown in the results reported in Figure 2, LNP₁₀ and LNP₂₀ exhibited positive zeta-potential, small sizes ranging from 120 to 130 nm, and adequate polydispersity index (PDI = 0.12 and 0.27, respectively). The DNA encapsulation efficiency for LNP formulations was larger than 60% (details are reported in Figure S1 in the Supplementary Materials).

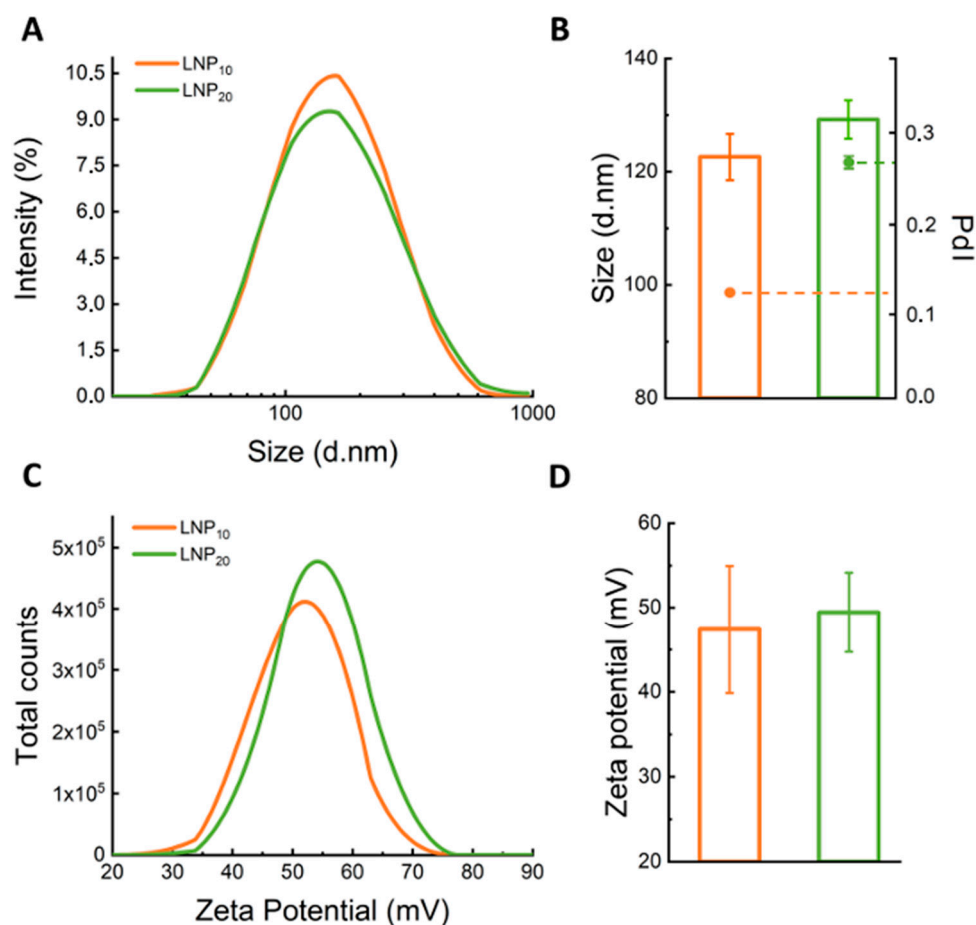


Figure 2. Size and zeta-potential of LNPs. (A) Size distributions, (B) mean size (reported as z-average) and polydispersity index (PDI) values, (C) zeta-potential distributions, and (D) average zeta-potential of LNP₁₀ (orange) and LNP₂₀ (green).

The previous literature has recognized that the nanoscale structure of lipoplexes is critical for the mechanism by which they promote intracellular delivery of DNA [11], and the investigation of their structure–activity relationship has been the subject of many theoretical and experimental studies [12,24–26]. Mechanistic understanding of lipoplex–cell interactions led to the development of optimized formulations with superior TE even in hard-to-transfect cells [16] where the Lipofectamine™ transfection gold standard failed. On the other side, this basic knowledge has not been developed for LNPs yet, but it is mandatory for the development of optimized formulations [27]. Most studies have explored the nanostructure of siRNA- and mRNA-LNPs by SAXS. While there is consensus that RNA is positioned within the particle interior, understanding of the nanoscale organization of lipids and RNA by SAXS remains elusive. Depending on compositional and operating factors, different arrangements have been reported, such as multilamellar structures [28], Ia3d and Pm3n cubic phases [29], and other non-lamellar phases where RNA molecules are confined within aqueous cylinders [30].

In the present investigation, the nanostructures of LNP₁₀ and LNP₂₀ were characterized by TEM and synchrotron SAXS. The representative TEM image reported in Figure 3A shows that LNPs are spherically shaped with a size around 100 nm, in agreement with the DLS results reported in Figure 2. Synchrotron SAXS curves exhibited two broad Bragg peaks, located at $q_{001} = 0.91 \text{ nm}^{-1}$ and $q_{002} = 1.80 \text{ nm}^{-1} \approx 2 q_{001}$ (Figure 3B).

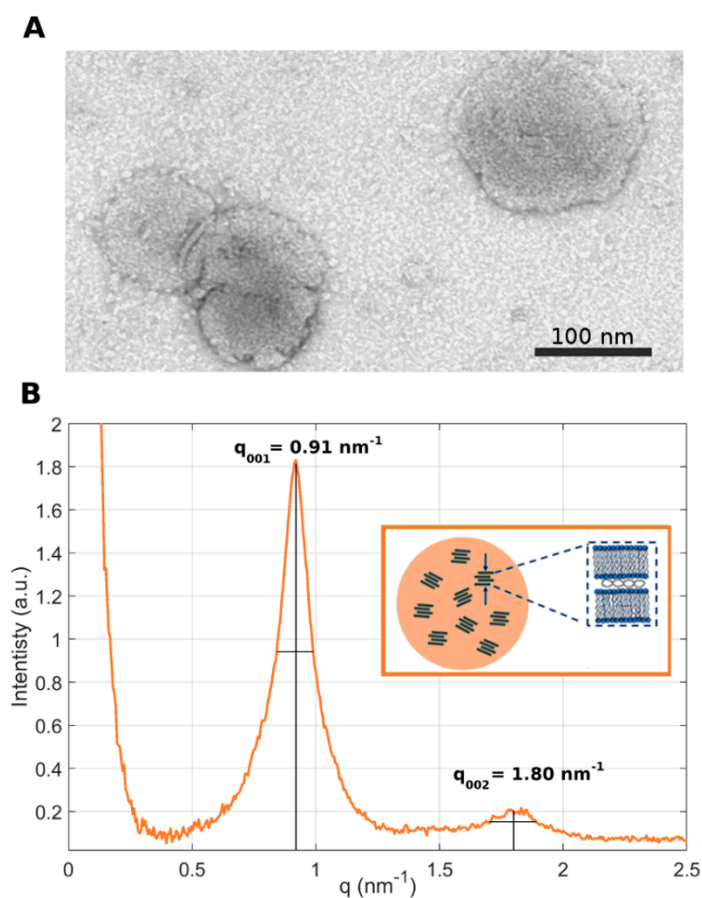


Figure 3. Nanostructure of LNPs. (A) Representative TEM image of LNP₁₀ (panel A) (scale bar = 100 nm). (B) Synchrotron SAXS pattern of LNP₁₀. The peaks arose from the lamellar periodicity of the system along the normal direction to the lipid bilayer. The small persistence length suggests that LNPs are made of randomly oriented lamellar domains, as schematically depicted in the inset. An average domain size made of 6 repeated units was estimated by relating the location of the first-ordered Bragg peak with its full width at half maximum (FWHM).

The presence of Bragg peaks is due to the lamellar periodicity of the system along the normal direction to the lipid bilayer. The length d of a single repeating unit in the lattice can be calculated as $d = 2\pi/q_{001} = 6.9$ nm and corresponds to the sum of the bilayer thickness (d_B) and the thickness of the water/DNA layer (d_W). More repeating units constitute a domain. By employing the Debye–Scherrer relation, the average domain size L_m was measured, i.e., $L_m = 2\pi/\Delta q_{001}$, where Δq_{001} is the full width at half maximum of the first-order Bragg peak. We obtained $L_m = 42.7$ nm, which corresponds to multiple short-range domains made of $n = L_m/d \approx 6$ repeating units. These results are in agreement with previous findings, according to which the internal structure of the LNPs is due to the arrangement of locally ordered domains along the normal direction to the lipid bilayer but randomly oriented along one particle radius [10] (Figure 3B, inset). This nanoscale arrangement of LNPs is less ordered than that of multilamellar “onion-like” lipoplex [31] complexes made of the same lipid species and also at the same lipid molar ratio and lipid/DNA ratio. Another distinctive feature of the SAXS pattern of the LNPs is the absence of the broad diffraction peak that is typically observed in the SAXS pattern of lipoplexes. That peak, referred to as the “DNA peak” [32], is usually located between the (001) and the (002) Bragg peaks and arises from a one-dimensional in-plane DNA–DNA lattice. Its absence in the SAXS trace of Figure 3B suggests that DNA is less densely packed in LNPs than in lipoplexes. This less ordered nanoscale organization may be more easily disintegrated upon interaction with cellular membranes and could contribute to explaining

the disassembly ability of the LNPs [33]. The next step was the *in vitro* validation of LNP₁₀ and LNP₂₀. To this end, we used human embryonic kidney 293 (HEK-293) and Chinese hamster ovary (CHO) cell lines that are frequently used in biological research. As the reproducibility of experimental data is a critical issue affecting the inconsistency of TE reports, user variability was assessed first. Results reported in Figure S2 in the Supplementary Materials demonstrated the high reproducibility of TE data. Figure 4 displays TE and cell viability of LNP₁₀ and LNP₂₀ in HEK-293 and CHO cells. The LNP formulations were as efficient as Lipofectamine™ 3000 in transfecting both cell lines. These findings are remarkable since Lipofectamine is the gold standard of transfection reagents with exceptional TE due to its virus-like intracellular trafficking behavior [25]. As the next step, LNPs were administered to HEK-293 and CHO cells and the cell viability was measured after 48 h. LNP₁₀ was found to have a minor effect on cell viability, while LNP₂₀ produced significant cytotoxicity (Figure 4C). The higher cytotoxicity of LNP₂₀ than LNP₁₀ is likely related to its higher dose of cationic lipids that can cause several changes to cells, such as cell shrinking, reduced number of mitoses, and vacuolization of the cytoplasm [34].

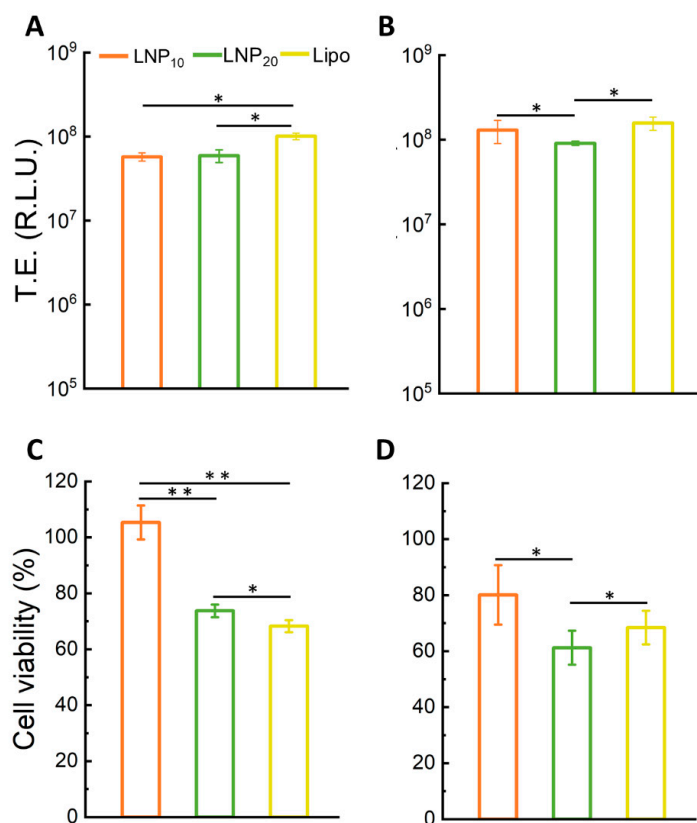


Figure 4. Transfection efficiency and cell viability of LNPs. Transfection efficiency (TE) of LNP₁₀ and LNP₂₀ expressed as relative light units (RLU) for HEK-293 (A) and CHO (B) cells. Cell viability of HEK-293 cells (C) and CHO cells (D) after treatment with LNP₁₀ and LNP₂₀ expressed as a percentage with respect to untreated cells. Statistical significance was evaluated using Student's *t*-test: * $p < 0.05$; ** $p < 0.01$ (no asterisk means lack of significance). Lipofectamine™ 3000 was used as a control.

According to TE and cell viability results, LNP₁₀ was selected as the best candidate for the delivery of a DNA vaccine. The chemical–physical stability of LNP₁₀ was assessed for up to 15 days through DLS measurements. In this timescale, the Z-potential of LNP₁₀ fluctuated between 35 and 45 mV, whereas its size increased from 160 to 240 nm (Figure S3A). This resulted in a slight decrease in the transfection efficiency (Figure S3B). To better elucidate the transfection behavior of LNP₁₀, we performed fluorescence confocal microscopy analysis of its uptake in cells (Figure 5). Texas Red–labeled LNP₁₀ were administered to HEK-293 and CHO cells to study their structural and dynamics properties using spatiotem-

poral correlation spectroscopy in the form of imaging-derived mean square displacement (iMSD) analysis, a technique capable of providing the average diffusion coefficient and dimension of fluorescent LNPs [17,18]. From fitting the iMSD curves (Figure 5A), the retrieved diffusion coefficient was found to be similar in CHO and HEK-293 cells and with an absolute value (i.e., $\sim 10^{-4} \mu\text{m}^2/\text{s}$) that describes quite immobile structures with respect to other cytoplasmic organelles (Figure 5B). Similarly, the average size of the Texas Red-LNP₁₀, calculated by the y -axis intercept of iMSD curves, is comparable between the two cell lines (Figure 5C) and corresponds to micrometric aggregates distributed near the cell membranes in both cases (Figure 5D). This evidence, in addition to being in accordance with the low diffusivity described above, is in keeping with data collected on other lipid-based systems with high fusogenic properties [35].

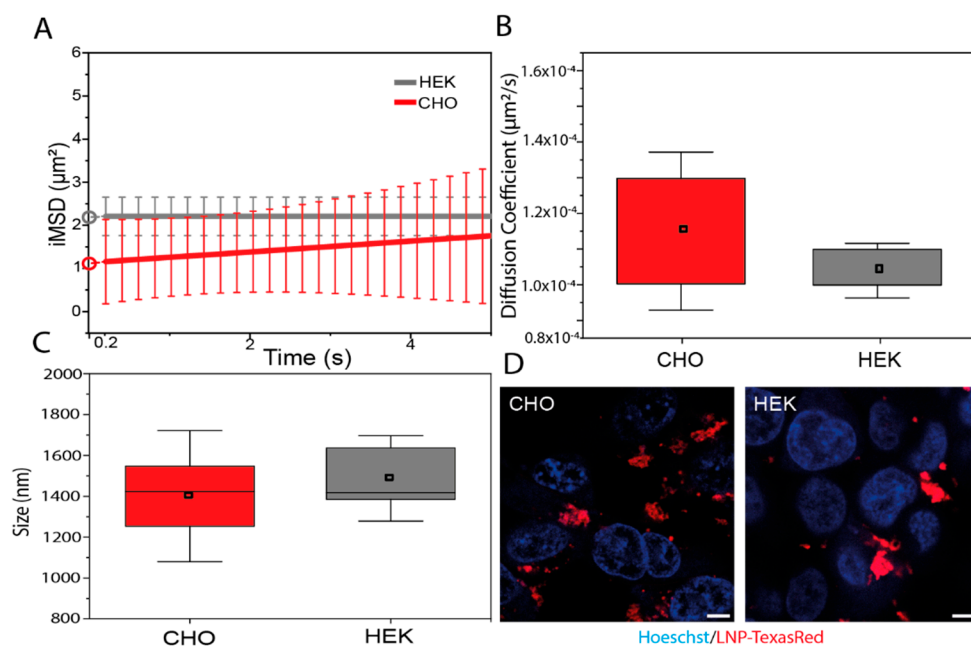


Figure 5. Intracellular behavior of LNPs. (A) Average iMSD curves of LNP-Texas Red in CHO (red, $n = 6$) and HEK cells (grey, $n = 6$). y -Axis intercept derived by fitting (circles) represents the average dimension of LNP-Texas Red clusters adhering to the plasma membrane. (B) iMSD-derived diffusion coefficients of LNP-Texas Red in CHO (red) and HEK-293 (grey). Boxes represent 25th–75th percentiles; whiskers represent standard deviation. (C) iMSD-derived size of LNP-Texas Red clusters in CHO (red) and HEK-293 (grey). Boxes represent 25th–75th percentiles; whiskers represent maximum–minimum ranges; lines represent median values. (D) Exemplary images of CHO and HEK-293 cells labeled with Hoechst (blue, for nuclei) and incubated with LNP-Texas Red (red). Scale bar = 5 μm .

To assess the ability of LNP₁₀ to deliver cancer vaccines, we prepared a variant of LNP₁₀ encapsulating pVAX-hECTM, a DNA vaccine conceived against the oncogene HER2 and known to be able to elicit a protective immune response against HER2-positive breast cancer in preclinical models [15]. HER2 is a tyrosine kinase receptor overexpressed in roughly 20% of breast cancer patients and correlates with poor prognosis [36]. HER2 is considered an optimal target for cancer immunotherapies since it is expressed on the cell membrane, and thus it can be targeted by antibodies and cell-mediated immunity. Antibodies can directly inhibit the signaling pathways downstream HER2 or mediate indirect reactions, such as antibody-dependent cell and complement-mediated cytotoxicity. The advent of the HER2 monoclonal antibody trastuzumab improved the overall survival and time-to-disease progression of patients with HER2-positive breast cancer [37]. However, many patients do not benefit from treatment because of therapy resistance. In this scenario, anti-HER2 DNA vaccination represents a promising alternative strategy, but its clinical

efficacy needs to be improved. The optimization of DNA vaccine delivery systems represents a key point to address. LNPs can improve the immunogenicity of the carried DNA vaccines and facilitate their administration. HER2 comprises an extracellular (EC) domain of 654 amino acids that contains four subdomains (I/L1, II/CR1, III/L2, and IV/CR2), a single transmembrane-spanning domain (TM), and a long cytoplasmic tyrosine kinase domain (IC). pVAX-hECTM encodes a truncated version of the human HER2 protein, encoding the EC and TM domains but lacking the IC domain [15].

To assess the ability of LNP₁₀ to deliver DNA vaccines, HEK-293 cells were transiently transfected with pVAX-hECTM encapsulated into LNP₁₀, and the expression of the encoded HER2 antigen was verified first by flow cytometry (Figure 6A,B) and then by immunofluorescence assay (Figure 6C,D) using the anti-human HER2 monoclonal antibody trastuzumab.

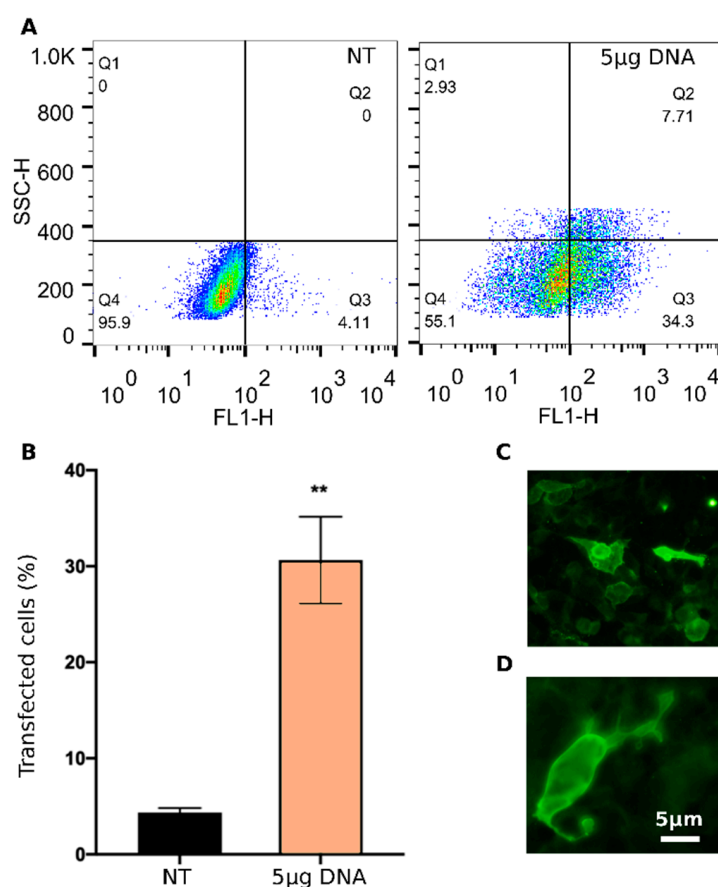


Figure 6. Transfection efficiency of LNP₁₀ carrying the anti-HER2 DNA vaccine pVAX-hECTM. (A) Representative dot plots (increasing dot density from blue to red) and (B) bar graphs showing the percentage of HER2-positive HEK-293 cells at 48 h post-transfection with pVAX-hECTM encapsulated into LNP₁₀ (5 µg DNA/well) in comparison with non-treated (NT) cells and analyzed by flow cytometry. Error bars represent average \pm S.D. ($n = 6$) ** $p < 0.001$ unpaired t -test. (C,D) Fluorescence microscope photographs of HEK-293 cells at 48 h post-transfection with pVAX-hECTM delivered by LNP₁₀ (10 \times and 40 \times magnifications in C and D, respectively). (NT: non-treated cells).

FACS analysis demonstrates that LNP₁₀ efficiently delivers pVAX-hECTM into HEK-293 cells, leading to 30% transfected cells. The immunofluorescence assay confirms that HEK-293 cells were able to ectopically express the target antigen after transfection by LNP₁₀. In particular, the strong membrane fluorescence signal observed in the transfected HEK-293 cells indicates that the HER2 antigen is exposed at the cell membrane as required for the induction of a protective antibody response [38].

4. Conclusions

Technological issues have limited the development of DNA vaccines for cancer so far. LNPs may help to address these issues and are now considered one of the most advanced delivery technologies. Using a screening strategy based on the physical–chemical characterization, and in vitro validation, we developed an LNP formulation with a distinct ability to transfect cell model lines as efficiently as Lipofectamine™ 3000. A variant of this formulation loaded with a DNA vaccine conceived against the oncogene HER2 produced a massive expression of the HER2 antigen on the cell membrane of the HEK-293 cells. Our results provide new insights into the structure–activity relationship of DNA-loaded LNPs and may contribute to lifting this gene delivery technology from basic knowledge to preclinical studies.

Supplementary Materials: The following supporting information can be downloaded at: <https://www.mdpi.com/article/10.3390/pharmaceutics14081698/s1>. Table S1: Size, zeta-potential, and polydispersity index (Pdl) of LNP₅, LNP₁₀, and LNP₂₀. Figure S1: (A) Calibration curve (black points) obtained through fluorescence signal measurement of pDNA and the related fluorescence signals obtained from LNP₁₀ and LNP₂₀ before and after treatment with Triton X-100 for measuring non-encapsulated pDNA and total pDNA amounts. (B) Encapsulation efficiency of pDNA within LNP₁₀ and LNP₂₀ calculated as reported in the Materials and Methods section. Figure S2: (A) Transfection efficiency (TE) of LNP₁₀, LNP₂₀, and Lipofectamine™ 3000 was measured by two users (indicated as “User 1” and “User 2”) in independent experiments. (B) High reproducibility of transfection data was demonstrated by linear regression of measured TE values. Figure S3: (A) Size (black) and Z-potential (grey) of LNP₁₀ measured at different time points (0, 5, 10, and 15 days). (B) Transfection efficiency (TE) of LNP₁₀ on HEK-293 cells measured at 0 and 15 days, expressed as relative light units (RLU) per mg of proteins.

Author Contributions: Conceptualization, A.A., C.M., D.P. and G.C.; methodology, H.A., L.M. and R.B.; software, L.D.; validation, L.C., S.R., E.Q. and J.W.; formal analysis, H.A., L.D., L.M. and R.B.; investigation, L.C., S.R., E.Q., J.W. and G.F.; resources, H.A., L.M., R.B., D.P. and G.C.; data curation, L.D., L.C., S.R., E.Q. and J.W.; writing—original draft preparation, S.R., F.C., C.M., and G.C.; writing—review and editing, F.C., C.M. and G.C.; visualization, C.M. and G.C.; supervision, A.A., C.M., F.C., D.P. and G.C.; project administration, A.A., C.M., D.P. and G.C.; funding acquisition, G.C. All authors have read and agreed to the published version of the manuscript.

Funding: The research leading to the results reviewed here received funding from the Sapienza University of Rome and from the Italian Minister for University and Research (MUR) for the research project “TITAN (Nanotecnologie per l’immunoterapia dei tumori)-Programma PON «R&I» 2014–2020 (ARS01_00906)”.

Institutional Review Board Statement: Not applicable.

Informed Consent Statement: Not applicable.

Data Availability Statement: Data reported in this study are available on request to the corresponding authors.

Conflicts of Interest: The authors declare no conflict of interest.

References

1. Siegel, R.L.; Miller, K.D.; Fuchs, H.E.; Jemal, A. Cancer statistics, 2022. *CA Cancer J. Clin.* **2022**, *72*, 7–33. [[CrossRef](#)] [[PubMed](#)]
2. Vanni, G.; Pellicciaro, M.; Materazzo, M.; Pedini, D.; Portarena, I.; Buonomo, C.; Perretta, T.; Rizza, S.; Pistolesse, C.A.; Buonomo, O.C. Advanced stages and increased need for adjuvant treatments in breast cancer patients: The effect of the one-year COVID-19 pandemic. *Anticancer Res.* **2021**, *41*, 2689–2696. [[CrossRef](#)] [[PubMed](#)]
3. Vardy, J.L.; Liew, A.; Warby, A.; Elder, A.; Keshet, I.; Devine, R.; Ouliaris, C.; Renton, C.; Tattersall, M.H.; Dhillon, H.M. On the receiving end: Have patient perceptions of the side-effects of cancer chemotherapy changed since the twentieth century? *Support. Care Cancer* **2022**, *30*, 3503–3512. [[CrossRef](#)]
4. Kraehenbuehl, L.; Weng, C.-H.; Eghbali, S.; Wolchok, J.D.; Merghoub, T. Enhancing immunotherapy in cancer by targeting emerging immunomodulatory pathways. *Nat. Rev. Clin. Oncol.* **2022**, *19*, 37–50. [[CrossRef](#)]
5. Abbaspour, M.; Akbari, V. Cancer vaccines as a targeted immunotherapy approach for breast cancer: An update of clinical evidence. *Expert Rev. Vaccines* **2022**, *21*, 337–353. [[CrossRef](#)] [[PubMed](#)]

6. Das, S.S.; Moitra, I.; Singh, S.K.; Verma, P.; Swain, S. DNA vaccines for cancer treatment: Challenges and promises. In *Nanotherapeutics in Cancer Vaccination and Challenges*; Elsevier: Amsterdam, The Netherlands, 2022; pp. 259–278.
7. Porter, K.R.; Raviprakash, K. DNA Vaccine Delivery and Improved Immunogenicity. *Curr. Issues Mol. Biol.* **2017**, *22*, 129–138. [[CrossRef](#)] [[PubMed](#)]
8. Young, J.L.; Dean, D.A. Electroporation-mediated gene delivery. *Adv. Genet.* **2015**, *89*, 49–88. [[PubMed](#)]
9. Zuidam, N.J.; Hirsch-Lerner, D.; Margulies, S.; Barenholz, Y. Lamellarity of cationic liposomes and mode of preparation of lipoplexes affect transfection efficiency. *Biochim. Biophys. Acta (BBA)-Biomembr.* **1999**, *1419*, 207–220. [[CrossRef](#)]
10. Quagliarini, E.; Renzi, S.; Digiaco, L.; Giulimondi, F.; Sartori, B.; Amenitsch, H.; Tassinari, V.; Masuelli, L.; Bei, R.; Cui, L. Microfluidic formulation of DNA-loaded multicomponent lipid nanoparticles for gene delivery. *Pharmaceutics* **2021**, *13*, 1292. [[CrossRef](#)] [[PubMed](#)]
11. Marchini, C.; Pozzi, D.; Montani, M.; Alfonsi, C.; Amici, A.; Amenitsch, H.; Candeloro De Sanctis, S.; Caracciolo, G. Tailoring lipoplex composition to the lipid composition of plasma membrane: A Trojan horse for cell entry? *Langmuir* **2010**, *26*, 13867–13873. [[CrossRef](#)]
12. Caracciolo, G.; Pozzi, D.; Caminiti, R.; Marchini, C.; Montani, M.; Amici, A.; Amenitsch, H. Enhanced transfection efficiency of multicomponent lipoplexes in the regime of optimal membrane charge density. *J. Phys. Chem. B* **2008**, *112*, 11298–11304. [[CrossRef](#)]
13. Caracciolo, G.; Pozzi, D.; Caminiti, R.; Amenitsch, H. Lipid mixing upon deoxyribonucleic acid-induced liposomes fusion investigated by synchrotron small-angle x-ray scattering. *Appl. Phys. Lett* **2005**, *87*, 133901. [[CrossRef](#)]
14. Marchini, C.; Pozzi, D.; Montani, M.; Alfonsi, C.; Amici, A.; Candeloro De Sanctis, S.; Digman, M.A.; Sanchez, S.; Gratton, E.; Amenitsch, H.; et al. Role of temperature-independent lipoplex–cell membrane interactions in the efficiency boost of multicomponent lipoplexes. *Cancer Gene Ther.* **2011**, *18*, 543–552. [[CrossRef](#)] [[PubMed](#)]
15. Quaglino, E.; Mastini, C.; Amici, A.; Marchini, C.; Iezzi, M.; Lanzardo, S.; De Giovanni, C.; Montani, M.; Lollini, P.-L.; Masucci, G. A better immune reaction to ErbB-2 tumors is elicited in mice by DNA vaccines encoding rat/human chimeric proteins. *Cancer Res.* **2010**, *70*, 2604–2612. [[CrossRef](#)] [[PubMed](#)]
16. Palchetti, S.; Pozzi, D.; Marchini, C.; Amici, A.; Andreani, C.; Bartolacci, C.; Digiaco, L.; Gambini, V.; Cardarelli, F.; Di Rienzo, C. Manipulation of lipoplex concentration at the cell surface boosts transfection efficiency in hard-to-transfect cells. *Nanomed. Nanotechnol. Biol. Med.* **2017**, *13*, 681–691. [[CrossRef](#)] [[PubMed](#)]
17. Ferri, G.; Digiaco, L.; D’Autilia, F.; Durso, W.; Caracciolo, G.; Cardarelli, F. Time-lapse confocal imaging datasets to assess structural and dynamic properties of subcellular nanostructures. *Sci. Data* **2018**, *5*, 1–8. [[CrossRef](#)] [[PubMed](#)]
18. Digiaco, L.; D’Autilia, F.; Durso, W.; Tentori, P.M.; Caracciolo, G.; Cardarelli, F. Dynamic fingerprinting of sub-cellular nanostructures by image mean square displacement analysis. *Sci. Rep.* **2017**, *7*, 14836. [[CrossRef](#)]
19. Koltover, I.; Salditt, T.; Safinya, C. Phase diagram, stability, and overcharging of lamellar cationic lipid–DNA self-assembled complexes. *Biophys. J.* **1999**, *77*, 915–924. [[CrossRef](#)]
20. De Ilarduya, C.T.; Sun, Y.; Düzgüneş, N. Gene delivery by lipoplexes and polyplexes. *Eur. J. Pharm. Sci.* **2010**, *40*, 159–170. [[CrossRef](#)] [[PubMed](#)]
21. Muñoz-Úbeda, M.; Misra, S.K.; Barrán-Berdón, A.L.; Aicart-Ramos, C.; Sierra, M.B.; Biswas, J.; Kondaiah, P.; Junquera, E.; Bhattacharya, S.; Aicart, E. Why Is Less Cationic Lipid Required to Prepare Lipoplexes from Plasmid DNA than Linear DNA in Gene Therapy? *J. Am. Chem. Soc.* **2011**, *133*, 18014–18017. [[CrossRef](#)]
22. Felgner, P.L.; Gadek, T.R.; Holm, M.; Roman, R.; Chan, H.W.; Wenz, M.; Northrop, J.P.; Ringold, G.M.; Danielsen, M. Lipofection: A highly efficient, lipid-mediated DNA-transfection procedure. *Proc. Natl. Acad. Sci. USA* **1987**, *84*, 7413–7417. [[CrossRef](#)] [[PubMed](#)]
23. He, C.; Hu, Y.; Yin, L.; Tang, C.; Yin, C. Effects of particle size and surface charge on cellular uptake and biodistribution of polymeric nanoparticles. *Biomaterials* **2010**, *31*, 3657–3666. [[CrossRef](#)] [[PubMed](#)]
24. Ewert, K.; Evans, H.M.; Ahmad, A.; Slack, N.L.; Lin, A.J.; Martin-Herranz, A.; Safinya, C.R. Lipoplex Structures and Their Distinct Cellular Pathways. In *Advances in Genetics*; Academic Press: Cambridge, MA, USA, 2005; pp. 119–155.
25. Cardarelli, F.; Digiaco, L.; Marchini, C.; Amici, A.; Salomone, F.; Fiume, G.; Rossetta, A.; Gratton, E.; Pozzi, D.; Caracciolo, G. The intracellular trafficking mechanism of Lipofectamine-based transfection reagents and its implication for gene delivery. *Sci. Rep.* **2016**, *6*, 25879. [[CrossRef](#)]
26. Pozzi, D.; Marchini, C.; Cardarelli, F.; Amenitsch, H.; Garulli, C.; Bifone, A.; Caracciolo, G. Transfection efficiency boost of cholesterol-containing lipoplexes. *Biochim. Biophys. Acta (BBA)-Biomembr.* **2012**, *1818*, 2335–2343. [[CrossRef](#)]
27. Papi, M.; Pozzi, D.; Palmieri, V.; Caracciolo, G. Principles for optimization and validation of mRNA lipid nanoparticle vaccines against COVID-19 using 3D bioprinting. *Nano Today* **2022**, *43*, 101403. [[CrossRef](#)]
28. Viger-Gravel, J.; Schantz, A.; Pinon, A.C.; Rossini, A.J.; Schantz, S.; Emsley, L. Structure of lipid nanoparticles containing siRNA or mRNA by dynamic nuclear polarization-enhanced NMR spectroscopy. *J. Phys. Chem. B* **2018**, *122*, 2073–2081. [[CrossRef](#)] [[PubMed](#)]
29. Martínez-Negro, M.; Kumar, K.; Barrán-Berdón, A.L.; Datta, S.; Kondaiah, P.; Junquera, E.; Bhattacharya, S.; Aicart, E. Efficient cellular knockdown mediated by siRNA nanovectors of gemini cationic lipids having delocalizable headgroups and oligo-xyethylene spacers. *ACS Appl. Mater. Interfaces* **2016**, *8*, 22113–22126. [[CrossRef](#)] [[PubMed](#)]

30. Yanez Arteta, M.; Kjellman, T.; Bartesaghi, S.; Wallin, S.; Wu, X.; Kvist, A.J.; Dabkowska, A.; Székely, N.; Radulescu, A.; Bergenholtz, J. Successful reprogramming of cellular protein production through mRNA delivered by functionalized lipid nanoparticles. *Proc. Natl. Acad. Sci. USA* **2018**, *115*, E3351–E3360. [[CrossRef](#)]
31. Caracciolo, G.; Amenitsch, H. Cationic liposome/DNA complexes: From structure to interactions with cellular membranes. *Eur. Biophys. J.* **2012**, *41*, 815–829. [[CrossRef](#)]
32. Caracciolo, G.; Pozzi, D.; Amenitsch, H.; Caminiti, R. Multicomponent Cationic Lipid–DNA Complex Formation: Role of Lipid Mixing. *Langmuir* **2005**, *21*, 11582–11587. [[CrossRef](#)]
33. Hope, M.J. Enhancing siRNA delivery by employing lipid nanoparticles. *Ther. Deliv.* **2014**, *5*, 663–673. [[CrossRef](#)] [[PubMed](#)]
34. Fröhlich, E. The role of surface charge in cellular uptake and cytotoxicity of medical nanoparticles. *Int. J. Nanomed.* **2012**, *7*, 5577–5591. [[CrossRef](#)]
35. Di Santo, R.; Digiacomo, L.; Palchetti, S.; Palmieri, V.; Perini, G.; Pozzi, D.; Papi, M.; Caracciolo, G. Microfluidic manufacturing of surface-functionalized graphene oxide nanoflakes for gene delivery. *Nanoscale* **2019**, *11*, 2733–2741. [[CrossRef](#)]
36. Siegel, R.L.; Miller, K.D.; Fuchs, H.E.; Jemal, A. Cancer statistics, 2021. *CA Cancer J. Clin.* **2021**, *71*, 7–33. [[CrossRef](#)] [[PubMed](#)]
37. Mendes, D.; Alves, C.; Afonso, N.; Cardoso, F.; Passos-Coelho, J.L.; Costa, L.; Andrade, S.; Batel-Marques, F. The benefit of HER2-targeted therapies on overall survival of patients with metastatic HER2-positive breast cancer—A systematic review. *Breast Cancer Res.* **2015**, *17*, 1–14. [[CrossRef](#)] [[PubMed](#)]
38. Rolla, S.; Marchini, C.; Malinarich, S.; Quaglino, E.; Lanzardo, S.; Montani, M.; Iezzi, M.; Angeletti, M.; Ramadori, G.; Forni, G. Protective immunity against neu-positive carcinomas elicited by electroporation of plasmids encoding decreasing fragments of rat neu extracellular domain. *Hum. Gene Ther.* **2008**, *19*, 229–240. [[CrossRef](#)]